Design and Self-Assembly of Sugar-Based Amphiphiles: Spherical to Cylindrical Micelles

Pablo Argudo, Léa Spitzer, François Jerome, Henri Cramail, Luis Camacho, Sébastien Lecommandoux

Design and self-assembly of sugar-based amphiphiles: spherical to cylindrical micelles

Pablo G. Argudo,[1,‡,] Léa Spitzer,[1,2,‡], François Jerome,[2] Henri Cramail,[1] Luis Camacho,[3] Sébastien Lecommandoux,[1,*]*

[1]Univ. Bordeaux, CNRS, Bordeaux INP, LCPO, 16 Avenue Pey-Berland, 33600 Pessac, France

[2]Institut de Chimie des Milieux et Matériaux de Poitiers, CNRS-Université Poitiers, ENSIP, 1 rue Marcel Doré, 86073 Poitiers, France

[3]Departamento de Química Física y T. Aplicada, Instituto Universitario de Nanoquímica IUNAN, Facultad de Ciencias, Universidad de Córdoba (UCO), Campus de Rabanales, Ed. Marie Curie, 14071 Córdoba, Spain.

Abstract

Sugar-based amphiphiles are a relevant natural alternative to synthetic ones due to their biodegradable properties. The understanding of their structure-assembly relationship is needed to allow the concrete synthesis of suitable derivatives. Here, four different mannose-derivative surfactants are characterized by pendant drop, dynamic light scattering, small-angle X-ray scattering, cryo-transmission electron microscopy and molecular dynamics techniques in aqueous media. Measurements denote how the polysaccharide average degree of polymerization ($\overline{DP}$) and the addition of a hydroxyl group to the hydrophobic tail, and thus the presence of a second hydrophilic moiety, affect their self-assembly. A variation in the $\overline{DP}$ of the amphiphile has no effect in the critical micelle concentration in contrast to a change of the hydrophobic molecular region. Moreover, high $\overline{DP}$ amphiphiles self-assemble into spherical micelles irrespectively of the hydroxyl

group presence. Low $\overline{DP}$ ones with only one hydrophilic moiety form cylindrical micelles, while the addition of a hydroxyl group to the tail lead to a spherical shape.

1. Introduction

Amphiphiles are well-known molecules characterized by having two specific moieties: a hydrophilic "head" group and a hydrophobic "tail" region. These compounds are under constant research, focus, and development due to their wide applications in our society in the form of drug delivery systems[1], nanotemplates[2], detergents[3] or cosmetics[4]. Distinguished for their ability to self-assemble and stabilize interfaces while adding innate properties to the system, such as viscoelasticity[5], at present most of the surfactants found in the market are manufactured or synthesized from non-biodegradable petrochemical sources[6]. The discovery of new environmentally friendly supply routes is of vital importance due to the crude oil depletion. Thus, sugar-based surfactants are of particular interest due to their high biocompatibility and low environmental impact[7]. Bio-based amphiphiles not only provide us a way to decrease the environmental pollution produced during their obtention, but also in their application. In addition to their biodegradability, their properties such as wettability, surface activity, pH, salt or temperature resistance as well as biological recognition can provide addition relevant properties. As an example, rhamnolipids have proven their viability in eco-friendly formulations for hair washing and conditioning[8] while sophorolipids opened a new route in the development of control plant diseases as a result of their antimicrobial activity[9].

Above their critical micellar concentration (CMC), sugar-based amphiphiles can self-assemble into well-defined nanostructures. In an aqueous system, the hydrophobic region gets surrounded by its hydrophilic sugar counterpart, the polar group, which is in direct contact with the liquid media. This reorganization process is characterized by an entropy increase in the system and yields to a

thermodynamically favorable assembly[10]. The final conformation adopted can be related to the concentration of the system, the solvent used, and more importantly, the molecular structure of the amphiphile. The demand for specific nanostructures whose morphology and size can be adjusted is on the rise. Different studies have shown how their size[11] and their morphology[12] are directly related to biological recognition processes, as in cells and viruses. Thus, the design and understanding of specific environmentally-friendly amphiphiles with the desired properties is an imperative. Recent examples of several assembled structures based on sugar-based amphiphiles can be found in the literature. Galactose and glucose-based amphiphiles have been reported to self-assemble into spherical micelles[13,14], maltoside-derivatives organize in cylindrical micelles[15] and xylan-based ones in the form of vesicles[16]. While a wide characterization is supplied, further explanations between their molecular structure and self-assembly behavior are seldom and often incomplete[17]. General routes to target desired shape and size self-assembled glycosides are still needed. A better comprehension of their interfacial and bulk behavior would be beneficial and highly advantageous for their future design and implementation in the society. To date, the majority of the reported analysis of sugar-based amphiphiles focus on simple structures, with one to four sugar units[18,19]. Furthermore, most studies do not address the effect and influence of the hydrophobic region on the final conformation. Contributions are focused on the nature of the sugar units, while the lipophilic chain is 'reduced' to a nonpolar chain. Only some theoretical reports can be found with more complex moieties[20]. It is necessary to understand the role and effect of variations in the lipophilic-hydrophilic balance and solubility, a major problem in one-sugar surfactants, in the self-assembly process. Changes along all the molecular structure as a gradual increment of the sugar degree of polymerization ($\overline{DP}$) or an increase in the hydrophobic region complexity could provide further insights into their structure-behavior correlation. Recently, our group reported the environmentally-friendly synthesis of a mostly linear polar head mannose-based surfactant with variable $\overline{DP}$ ranking up to 8[21]. D-mannose is a natural monosaccharide widely used in the alimentary, cosmetic,

pharmaceutical, or medical fields. It can be used as a food supplement, biological recognition anchor in drug design or blocking colonization in animal feeds[22,23]. It is also directly involved in the biological recognition of mannan-binding lectins that form part of the immunity system and its application for biobased nanocarriers is of vital importance. Mannose receptors are also expressed on alveolar macrophages, target for the treatment of diseases such as tuberculosis, or possess a critical role in phagocytosis through C-type lectin membrane receptors[24].

Here, we present the self-assembly characterization of four mannose-derivative glycoside amphiphiles. Two almost linear mannose polysaccharides with different $\overline{DP}$ (= 3 and 8) were linked to an oleic or ricinoleic acid by click chemistry. Each amphiphilic derivative was characterized individually in order to understand its resulting self-assembly. In a systematic way, the effects of the $\overline{DP}$ in the final thermodynamically favorable structure, as well as the effect of a hydroxyl group at the unsaturated hydrophobic tail, in the case of the ricinoleic acid derivative, were studied. A comprehensive understanding of their organization at fluid interfaces was achieved and a plausible explanation reached. The air/water interface was analyzed as a simple and reliable way to elucidate the 2D self-assembly behavior of the amphiphiles[25]. Furthermore, a complete characterization of their 3D self-assembly above the CMC was performed. Bulk studies revealed how small-scale changes in the molecular structure of the amphiphile lead to discrete aqueous self-assembled formations[26]. The self-assembly capabilities of the amphiphiles are strongly correlated to their molecular composition. To conclude, guiding rules for the design of different micellar structures by the chemical modification of mannose-derivative surfactants for further applications are provided.

2. Experimental section

2.1. Materials. D-(+)-Mannose monosaccharides (from wood, ≥ 99%) and Amberlyst-15 (≥ 90%, 0.355 – 1.18 mm, 1.7 mL^{-1} capacity) were purchased from Sigma Aldrich and dried under vacuum conditions prior to their use. 1,6-Anhydro-β-D-mannopyranose and Propargyl α-D-mannopyranoside were obtained from Biosynth Carbosynth and used without purification. L-

Ascorbic acid (99%), propargyl alcohol (99%), D-Sorbitol (≥ 98%), 3-bromo-1-propanol (97%), 1,5,7-triazabicyclo[4.4.0]dec-5-ene (98%), sodium azide (≥99.5%), and N,O-Bis(trimethylsilyl)trifluoroacetamide (99%) were acquired from Sigma Aldrich and used without further purification. Methyl oleate (≥ 99.9%) was procured by Nuchekrep. Magnesium Sulfate ($MgSO_4$) was purchased from Sigma Aldrich. Cuprisorb and Copper(II) sulfate were obtained from Seachem and ProLabo, respectively. Chloroform, THF, acetone, petroleum ether, dimethyl sulfoxide (DMSO), acetonitrile, ethyl acetate, diethyl ether, and pyridine were purchased from Sigma Aldrich and used as obtained. Dialysis steps were realized using a Spectra/Por®6 MWCO 100-500 Da membrane. The ultrapure water used was produced by a Millipore Milli-Q unit and pretreated by a Millipore reverse osmosis system (>18.2 MΩ·cm).

2.2. Sample preparation. For pendant drop experiments, different concentration samples were prepared by the addition of the amphiphiles to previously filtered ultrapure water (using a 0.22 µm PTFE filter), in the range of 0.01 to 15 mmol·mL^{-1}. For DLS, Cryo-TEM and SAXS characterizations, samples were also prepared by direct dissolution. Surfactants were dispersed in previously filtered ultrapure water (using a 0.22 µm PTFE filter) at a concentration of 10 and 25 mmol·mL^{-1}, concentrations above the CMC. Solutions were magnetically stirred at 450 rpm for 24 h at room temperature and filtered twice through a 0.45 µm PTFE filter without a significant weight loss. Sample concentrations were calculated using the respective number-average molecular weight, $\overline{M_n}$, of each amphiphile.

2.3. Characterization methods

Nuclear Magnetic Resonance (NMR). A Bruker AVANCE III 400 (Bruker Scientific Instruments, Massachusetts, USA) equipped with a 5 mm probe was used. It was operated at 400.2 MHz for ^{1}H and 298 K. Samples within a 20-40 mg·mL^{-1} concentration range were measured using deuterated solvent (D_2O, Eurisotop; 99.0 atom % D, ^{1}H-NMR: δ = 4.8 ppm.). 128 scans were recorded, and

the data obtained were compiled using the Bruker Topspin software. The final spectra were analyzed by TopSpin (v. 4.0.9). Automatic phase correction and integration steps were applied.

Matrix-Assisted Laser Desorption/Ionisation-Time of flight (MALDI-TOF). A CESAMO (Bordeaux, France) on an Autoflex maX TOF mass spectrometer (Bruker Daltonics, Bremen, Germany) equipped with a frequency tripled Nd:YAG laser (355 nm) was used to record every spectrum. A 19 kV acceleration voltage in the positive-ion linear mode was needed. 1 mL vacuum-dried samples were measured at a concentration of 20 $mg \cdot mL^{-1}$ in water/acetonitrile 70/30 ratio with trifluoroacetic acid (10 vol%) solvent. A 10:1 v/v mixture of the samples with a 2,5-dihydroxybenzoic acid solution was prepared by the prior solution of 10 mg of it in 1 mL of acetonitrile.

Size Exclusion Chromatography (SEC). An Ultimate 3000 System (Thermoscientific) equipped with diode array detector, DAD, and a multi-angle laser light scattering detector MALLS (Wyatt Technology) was utilized for the determination of molar masses. In all samples, water was used as eluent. The separation of the compounds was carried out by two Shodex OH Pack 802.5 columns with exclusion limits from 500 Da to 10 000 Da. A temperature of 25 ºC and a flow rate of 0.6 $mL \cdot min^{-1}$ were applied. The number average molar mass, $\overline{M_n}$, weight average molar mass, $\overline{M_w}$, and dispersity, Đ, were calculated after calibration with dextran as standard.

Attenuated Total Reflectance Infrared Spectroscopy (ATR-IR). FTIR spectra were recorded on a Bruker VERTEX 70 instrument (DLaTGS MIR) equipped with a Pike GladiATR plate (diamond crystal). Each spectrum was obtained with a 4 cm^{-1} resolution after 64 scans at room temperature.

Tensiometry. A Drop Shape Analyzer-DSA100 (Krüss GmbH, Germany) using a CF04 camera (320 fps at 1200 × 600 px), a high-power monochromatic LED (λ = 470 nm) illumination, and a 0.72 mm diameter needle was used to obtain the surface tension data. Samples were prepared in an aqueous media and measured at 20 ± 0.5 ºC. Between three and six replicated experiments were done at each concentration and the average value is shown. For accurate results, the droplets were

measured in a sealed small cuvette in order to create an equilibrium humid atmosphere and slow the evaporation process[27].

Dynamic Light Scattering (DLS). A Zetasizer Nano ZS Instrument (Malvern Instruments Ltd., Malvern, UK) with a red line (wavelength, $\lambda = 632$ nm) of a He-Ne laser in a quasi-backscattering configuration (scattering angle, $\theta = 173°$) was used to evaluate the apparent diffusion coefficient, at 20 ºC. Moreover, to accurately corroborate the size distribution, multiangle light scattering analysis (ALV DLS) were also carried out using an ALV 22 mW linearly He-Ne polarized goniometer laser ($\lambda = 632$ nm) with an ALV-5000/EPP multiple tau digital correlator (initial sampling time 125 ns). Samples were analyzed at 20 ºC in an angle range from 30º to 150º.

Small Angle X-ray Scattering (SAXS). A Xeuss 2.0 (XENOCS, France) equipped with a Genix-3D Cu beam (K_α wavelength of 0.1542 nm) with a Dectris Pilatus-300k (Dectris, Switzerland) detector was used. The apparatus was operated at 40 kV and 40 mA with a sample distance of 1.635 m and an exposure time of 3 h per sample. A capillary made of quartz with an inner diameter of ~1.5 mm and 10 μm thickness was utilized as sample holder. The scattered X-ray intensities were collected in a two-dimensional position-sensitive imaging plate and integrated over a linear profile to convert into one-dimensional (I(q) vs. q) scattering data. Background scattering, obtained from MilliQ water, was subtracted from the sample data to obtain scattering just from the self-assembled structures.

Cryo-Transmission Electron Microscopy (cryo-TEM). A LaB6 JEOL 2100 (JEOL, Japan) cryo microscope was used to obtain the micrographs. It was operated with a JEOL low dose system (Minimum Dose System, MDS) at 200 kV to protect the sample ice film from any irradiation before imaging and reduce irradiation during image capture. An ultrascan 2k CCD camera (Gatan, USA) was employed to record the images and a “quantifoil” (Quantifoil Micro Tools GmbH, Germany) carbon membrane was used to prepare the thin films. A droplet was directly deposited on the substrate and any sample surplus on the membrane was removed while liquid ethane was employed

to quench-freeze and form the thin film. Samples were measured at -180 ºC in a Gatan 626 cryo-holder cooled with liquid nitrogen.

2.4. Simulation model and parameters.

Atomistic (ATM). Molecular mechanics (MM) and molecular dynamics (MD) calculations were performed using a Dreiding force field (Forcite). The charge was incorporated by Charge equilibration (QEq). A cutoff of 1.85 nm was used to calculate the Leonard-Jones (LJ) interactions and short-range electrostatic interactions. For each MD simulation, the procedure was started with a geometry optimization protocol followed by 400 ps of NVE ensemble dynamics with a 0.2 fs heating ramp from 300 K to 500 K. After, the geometry was again optimized by MM. MD-MM optimization cycles were repeated 10 times.

Coarse-Grained (CG) Martini force field. Self-assembly MD calculations were performed by using a Martini force field on a coarse-grained (CG) model (Mesocite). A cutoff of 1.0 nm was employed to calculate the LJ and short-range electrostatic interactions. Periodic boundary NPT MD calculations were carried out at a temperature of 293.15 K and 1 atm with a 2 fs time step to a total simulation of 500 ns.

3. Results and discussion

Four mannose-based (PMan) derivatives with differences in their polar head degree of polymerization ($\overline{DP_n}$ = 3 and 8) and in their nonpolar tail structure (based on oleic and ricinoleic fatty acids) have been investigated. The molecular structures of these amphiphiles are shown in **Figure 1.** The latter are composed of a mixture of oligomers and exhibit a dispersity, *Đ*, of *ca.* 2, as expected for a polycondensation synthesis. The tuning of their final intermolecular interactions was achieved by adjusting the length and complexity of the hydrophilic and hydrophobic counterparts, respectively. Note that the sugar-based polar head groups are not purely linear, presenting a main chain of mannose units connected via α-(1,6)-glycosidic linkage (60 %) with branching patterns at

the OH-2 position (24 %) and some other connections via β-(1,6) and β-(1,2) linkages (8 %). An in-depth description of the synthesis procedure of similar surfactants was already reported by the group[21] (see **Figure S1**-**S8**).

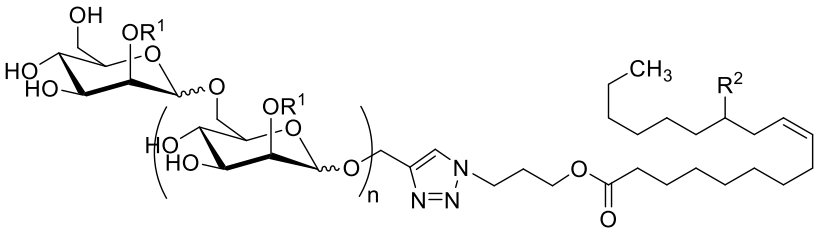

R1: H or mannose

n: 2, R2: H = (PMan)3-*b*-OI
n: 7, R2: H = (PMan)8-*b*-OI
n: 2, R2: OH = (PMan)3-*b*-Ric
n: 7, R2: OH = (PMan)8-*b*-Ric

Amphiphile name	$\overline{M_n}$[a] (g/mol)	Dispersity, D[b]	f_{Man} (%)[a]
$(PMan)_3$-*b*-OI	908	2.00	56
$(PMan)_8$-*b*-OI	1719	2.03	77
$(PMan)_3$-*b*-Ric	924	2.00	55
$(PMan)_8$-*b*-Ric	1725	2.03	76

[a]The number-average molecular weight ($\overline{M_n}$) and the hydrophilic weight ratio (f_{Man}) of the amphiphiles were determined by ^{1}H-NMR spectroscopy.
[b]Dispersity = Polar head PMan $\overline{M_w}/\overline{M_n}$; $\overline{M_w}$ and $\overline{M_n}$ were measured by SEC using H_2O as eluent and dextran as calibration standards at 25 °C

Figure 1. $(PMan)_n$-*b*-fatty acid derivatives: structure, chemical formula and molecular parameters overview.

The relationship between the molecular structure and self-assembly of each amphiphile at the air/water interface was investigated by measuring the equilibrium surface tension (γ) as a function of the concentration by the pendant drop technique. All the curves obtained are provided in **Figure S9**. Monodisperse samples are characterized by a linear decay until a plateau is reached. However, minimal changes in the system or the purity of the sample are known to affect the final interfacial data[28,29]. Due to the dispersity of the polar moiety and the possible formation of pre-micellar systems accounting to the strong hydrogen bonding ability of sugars, the surface tension decay as function of the concentration denoted a smoother decay than usual, making it harder to extract the accurate

CMC value[30]. Therefore, limitations of their analysis preclude analyzing these results as absolute values but rather as a general trend.

Table 1. Critical micelle concentration, surface tension and 10 mM hydrodynamic radius of $(PMan)_n$-*b*-fatty acid derivatives.

Sample	CMC (mM)	γ_{CMC} (mN/m)	R_h (nm) (DLS, ALV)	PDI (DLS, Malvern)
$(PMan)_3$-*b*-OI	1.54 ± 0.12	43.0 ± 0.2	13.3	0.19
$(PMan)_8$-*b*-OI	1.60 ± 0.17	47.1 ± 0.3	4.6	0.08
$(PMan)_3$-*b*-Ric	0.65 ± 0.10	39.4 ± 0.2	5.1	0.07
$(PMan)_8$-*b*-Ric	0.62 ± 0.11	41.8 ± 0.2	4.3	0.08

As it can be observed in **Table 1**, long-chain polar head amphiphiles $(PMan)_8$-*b*-OI and $(PMan)_8$-*b*-Ric denote similar average CMC values (*ca.* 1.60 and *ca.* 0.62 mM, respectively) than their short-chain counterparts $(PMan)_3$-*b*-OI (*ca.* 1.54 mM) and $(PMan)_3$-*b*-Ric (*ca.* 0.65 mM). Nevertheless, a general increase in the surface tension at the CMC (γ_{CMC}) was also observed for longer sugars. $(PMan)_8$-*b*-OI shows a higher γ_{CMC} value (*ca.* 47.1 mN/m) compared to $(PMan)_3$-*b*-OI (*ca.* 43.0 mN/m) and same increased tendency was distinguished for $(PMan)_8$-*b*-Ric (*ca.* 41.8 mN/m) compared to $(PMan)_3$-*b*-Ric (*ca.* 39.4 mN/m). It can be concluded that the increase in the number of mannose groups has close to no impact in the CMC while increasing the γ_{CMC}. Usually, it is assumed that an increase in the polar region is directly related to a H-bonding promotion. As a consequence, a higher stabilization in the bulk media generally leads to larger CMC values[31]. This is not always the case, especially for sugar-based surfactants. In agreement with earlier findings reported in the literature, a small $\overline{DP}$ increase of the sugar moiety, in the form of one or two residues, can have from no impact to even decrease the CMC [32–34]. Similar behavior was observed by Vanaken *et al.* (between β-D-Glu and β-D-Mal amphiphiles) or Minamikawa *et al.* (between β-Mal_2(Ger) and β-Mal_3(Ger) ones)[32,35], where no variation in the CMC and an increase in the γ_{CMC} resulted as a

function of the sugar length. The relationship between the number of sugar residues and micelle formation is found to be affected by many variables rather than by their hydrophilicity, steric hindrance[36], or the stereochemistry of the headgroup alone[37]. As suggested by previous authors for other sugar-based amphiphiles, mannose polysaccharides may prefer to interact between them rather than with the surrounding media, enhancing the sugar-sugar interactions *via* H-bonding. Head-head interactions can be in charge of balancing the hydrophilicity of the system while compensating the additional sterically hindrance, leading to favorable micellar structures that maintain the CMC constant. The impact on the CMC is less affected by the addition of one sugar unit to the polar head than a change in the alkyl chain length or conformation[20]. $(PMan)_3$-*b*-Ric (0.64 mM) and $(PMan)_8$-*b*-Ric (0.62 mM) denoted lower CMC values compared to their counterparts $(PMan)_3$-*b*-OI (1.54 mM) and $(PMan)_8$-*b*-OI (1.59 mM). Moreover, the effect in the structure of the hydroxyl group could be also observed in the γ_{CMC}, where $(PMan)_3$-*b*-Ric (39.4 mN/m) and $(PMan)_8$-*b*-Ric (41.8 mN/m) denoted lower surface tension values as opposed to $(PMan)_3$-*b*-OI (43.0 mN/m) and $(PMan)_8$-*b*-OI (47.1 mN/m), respectively. The existence of a *cis* double bond is known to affect the molecular assembly by disrupting the packing of the hydrophobic tails[38], while the presence of a hydroxyl group can be directly related to the final molecule packing and organization at the air/water interface[39]. Their implementation led to a reorganization of the molecules at the interface, mostly promoted by changes in the tail assembly. In this regard, the relationship between the γ_{CMC} and the tail bending has been already reported[40]. Conformational changes occurring at the air–water interface can be responsible for a more oriented hydrocarbon tail at the interface, and lower γ_{CMC}. This change could be explained by a tail reorientation in the presence of an OH group, making the molecule behave as a bipolar amphiphile. Surface-pressure area isotherms of ricinoleic acid and methyl ricinoleate have shown that the hydrophobic tail can be reorientated in function of the molecular area[41]. A bent organization was characterized by interactions between the subphase and the COO group with the hydroxyl group at high molecular areas (*ca.* 66 A^2) while a perpendicular

state was observed at lower ones (*ca.* 34 A^2). Oleic acid, however, denoted a preferable perpendicular state (*ca.* 33 A^2) with no clear phase transitions. Similar behavior could be present in the mannose derivatives, where OI and Ric tails are based on ricinoleic and oleic acid structures.

Above the CMC, the self-assembly behavior of the amphiphiles in water was also the target of study, and their size and shape were observed by dynamic light scattering (DLS). **Figure 2** exemplarily shows the respective $(PMan)_8$-*b*-OI and $(PMan)_3$-*b*-OI ALV DLS correlogram and size distribution plots. All curves are provided in **Figure S10** and **S11**.

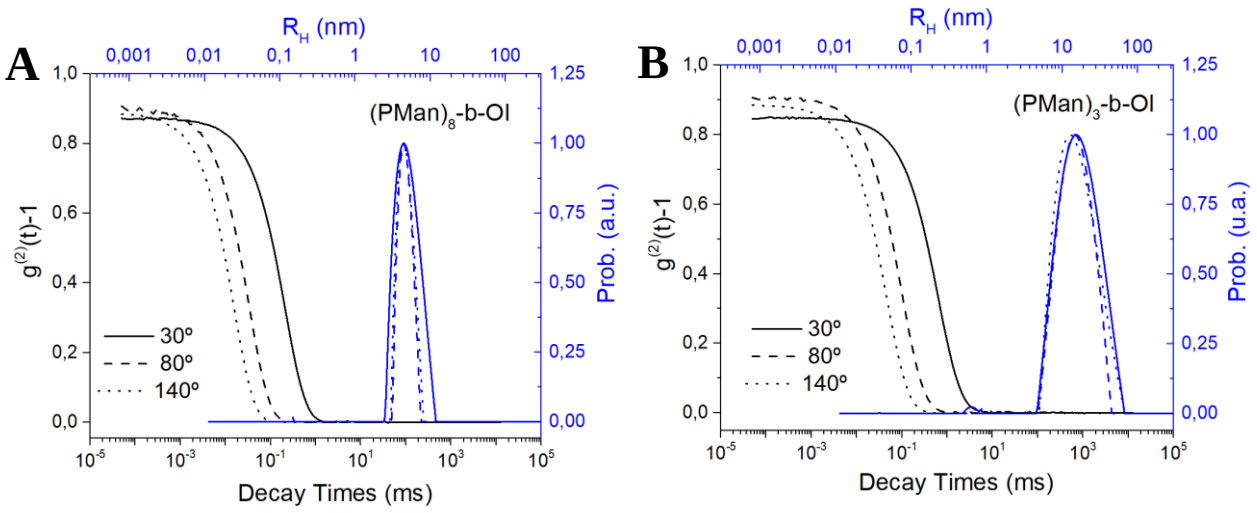

Figure 2. DLS intensity auto-correlation (black) and size distribution (blue) functions obtained by ALV at three different angles of 10 mM **(a)** $(PMan)_8$-*b*-OI and **(b)** $(PMan)_3$-*b*-OI.

As it can be observed in **Table 1**, $(PMan)_8$-*b*-OI and $(PMan)_8$-*b*-Ric, due to their large polar head group, form well-defined monodispersed micelles with an average R_h of *ca.* 4.6 and 4.3 nm, respectively (PDI = 0.08). Along the same lines but with a smaller $\overline{DP}$, $(PMan)_3$-*b*-Ric also shows a monomodal behavior of micelles with a slightly larger R_h of *ca.* 5.1 nm (PDI = 0.07). Multi-angle DLS experiments in the 30º to 150º range concluded that $(PMan)_8$ derivatives as well as $(PMan)_3$-*b*-Ric denote a purely diffuse scattering, confirming their spherical shape. **Figure S12** compiles the cumulant coefficient Γ values obtained as a function of the square of the wave vector q^2. Moreover, $(PMan)_8$-*b*-OI, $(PMan)_8$-*b*-Ric and $(PMan)_3$-*b*-Ric self-assemble into micelles with similar R_h values when increasing the sample concentration from 10 mM to 25 mM (**Figure S10)**. Comparing the size and conformation relationship of the amphiphiles at 10 mM, a slight variation of the micelles was observed between $(PMan)_8$-*b*-OI (4.6 nm) and $(PMan)_8$-*b*-Ric (4.3 nm) spherical self-assembly. The size of the micelles, with a $\overline{DP}$ of 8, is minimally affected by the molecular structure and the organization of the core. The slight R_h decrease of $(PMan)_8$-*b*-Ric can be associated to the OH group, which hydrophilicity could promote the tail bending due to the action of a second hydrophilic moiety, increasing the compactness of the core, compared to $(PMan)_8$-*b*-OI. Similar conclusion could be reached between $(PMan)_8$-*b*-Ric and $(PMan)_3$-*b*-Ric micelles, as their difference in concentration has no critical effect in the final conformation. While $(PMan)_8$-*b*-Ric molecules can organize their tail in a bent configuration due to the higher $\overline{DP}$, $(PMan)_3$-*b*-Ric amphiphiles can be described by a mostly vertical tail position. Thus, even if the sugar unit is smaller in average, the final size of the micelle is larger (5.1 nm) compared to $(PMan)_8$-*b*-Ric (4.3 nm). This conclusion would be in agreement with the literature, as reported between oleic and stearic-based surfactants, where the bending of the tail lead to smaller micelles[40]. More specifically, previous contributions evidenced how sodium ricinoleate derivatives, as $(PMan)_8$-*b*-Ric, can self-assemble into micelles where the OH group of the hydrophobic tail is in contact with the aqueous media or the CO, bending the hydrophobic tail[42]. This interpretation is in line with the previous 2D interfacial tensiometry

results, where the hydroxyl group is suggested to have a clear effect in the molecular reorganization. However, a different behavior was observed for the $(PMan)_3$-*b*-OI amphiphile. Self-assembled structures with a larger average R_h of 13.3 nm (PDI = 0.19) were obtained and associated with flexible cylindrical micelles. As for polymers, the R_h obtained was related with the folded state of the micelle, where an increase of the R_h with the concentration could be related to the increase of the cylindrical length of the micelles (**Figure S10**). A deeper analysis of the obtained DLS spectra also shows the presence of a second population with a smaller relaxation time, albeit in small concentrations, in the 5 nm range. The low population of spherical micelles could be associated with the presence of high $\overline{DP}$ molecules in the sample, due to the dispersity. As previously observed for $(PMan)_8$-b-OI, molecules with larger polar head groups are related to spherical conformations. In line with Israelachvili packing parameter $P = v_{tail}/(a_{hg}.l_{tail})$, (where v_{tail} is the volume of tail, a_{hg} is the head group area, and l_{tail} is the tail length), increased P values in molecules with only one hydrophilic moiety are associated with worm-like micelles, while smaller ones are to spherical micelles[43]. $(PMan)_8$-b-OI, due to its high $\overline{DP}$ and a_{hg}, is characterized by lower P values and thus assembles into spherical micelles. $(PMan)_3$-*b*-OI, in contrast to $(PMan)_3$-*b*-Ric, forms cylindrical structures that can be only explained by the absence of the hydroxyl group in the lipophilic tail. To assert the stability of the structures, the evolution of the self-assembled conformations was followed by DLS overtime during a period of 15 days. No change in the scattered intensity was observed, confirming the stability of the self-assembled micelles. **Figure S13** shows the micelle size distribution for all the sugar derivatives synthesized. It can be concluded that all the structures formed by the direct solubilization process are reproducible and thermodynamically stable in time.

A deeper view of these structures was obtained by cryo-TEM experiments. Spherical micellar self-assembled structures were observed for $(PMan)_8$-*b*-OI, $(PMan)_8$-*b*-Ric, and $(PMan)_3$-*b*-Ric in agreement with DLS results. In contrast, $(PMan)_3$-*b*-OI self-assembles into clear flexible cylindrical structures, while still in the presence of few small spherical micelles. **Figure 3** shows cryo-TEM

examples of the $(PMan)_8$-*b*-OI micellar and $(PMan)_3$-*b*-OI cylindrical assemblies (other significant cryo-TEM images can be found in **Figure S14)**. Also, shape stability could be observed in the studied range of the concentrations. Note that dark motives surrounded by a bright halo are ice aberrations produced during sample preparation. $(PMan)_3$-*b*-OI cylindrical micelles clarify the previous higher R_h and PDI DLS results obtained. Their values can be associated with the rotational and translational diffusion of flexible cylinders. Moreover, the small presence of spherical micelles can be directly related to the second distribution previously mentioned in the DLS spectrum, based on the presence of higher $\overline{DP}$ molecules in the sample.

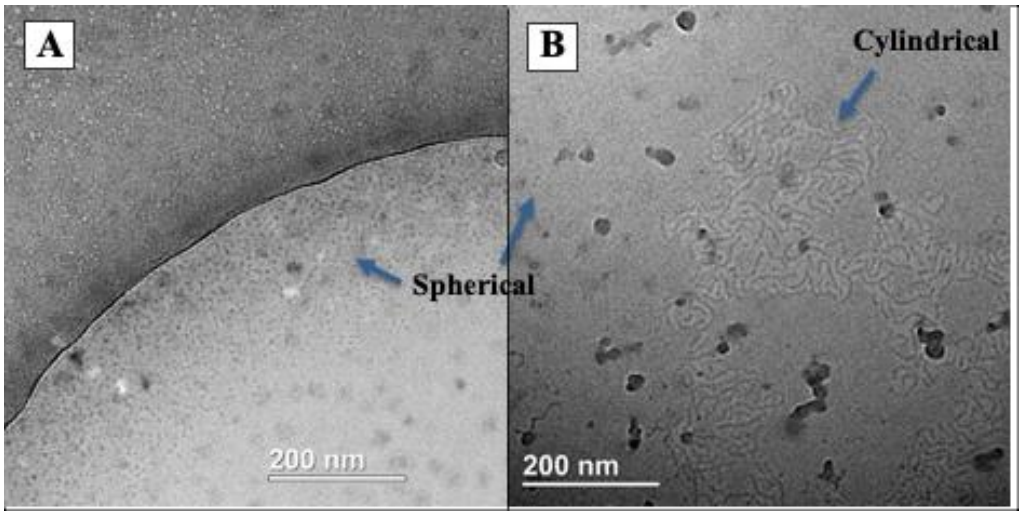

Figure 3. Cryo-EM images of **(a)** $(PMan)_8$-*b*-OI spherical micelles **(b)** $(PMan)_3$-*b*-OI cylindrical micelles. Darker motives surrounded by a bright halo are ice aberrations produced during sample preparation.

A complete morphological study of the sugar-based self-assembled structures, was carried out by small angle X-ray scattering (SAXS) measurements. **Figure 4** shows the experimental spectra of $(PMan)_8$-*b*-OI, $(PMan)_8$-*b*-Ric, $(PMan)_3$-*b*-Ric and $(PMan)_3$-*b*-OI self-assembled micelles. For all compounds, a characteristic dependence of the scattered intensity I(q) as a function of the wavevector q could be observed, from which fit it can be inferred the presence of well-defined nanostructures[44,45]. In the case of spherical micelles, the plateau at low q values can be fitted by a

Guinier Law, their R_g deduced and the R_g/R_h ratio can be used to get information of the micellar system[46]. $(PMan)_8$-*b*-OI, $(PMan)_8$-*b*-Ric, and $(PMan)_3$-*b*-Ric amphiphiles are described by R_g/R_h ratios of 0.78, 0.79, and 0.75, respectively, close to 0.77, ratio associated to perfect spherical micellar conformations[47,48].

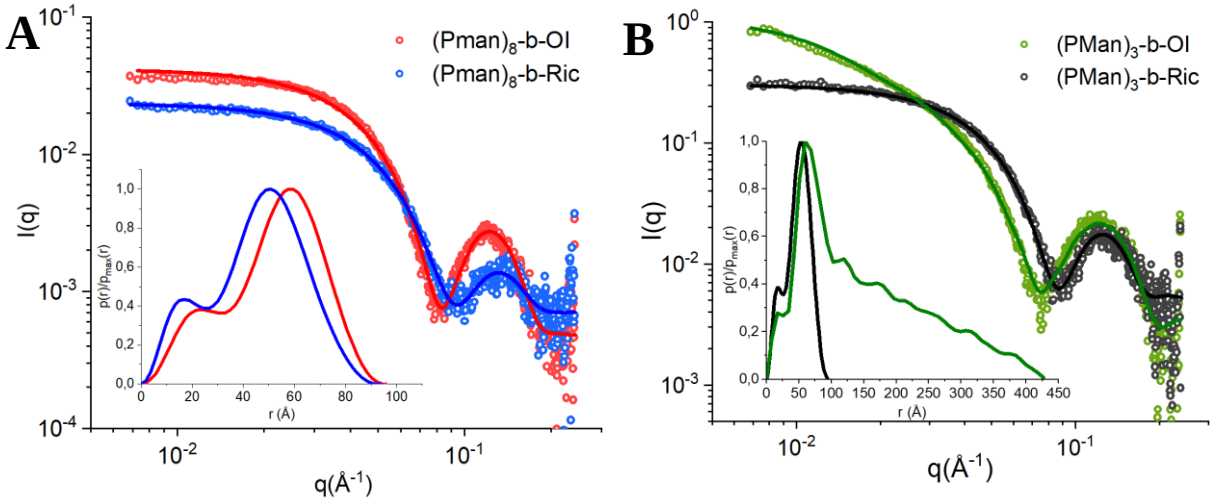

Figure 4. Small-Angle X-ray scattering signal (dots) and their respective spherical core/shell fitting (solid line) of **(a)** 10 mM $(PMan)_8$-*b*-OI (red) and $(PMan)_8$-*b*-Ric (blue) **(b)** 25 mM $(PMan)_3$-*b*-Ric (black) and $(PMan)_3$-*b*-OI (green). Inserted plots are the corresponding Pair Distance Distributions Functions (PDDF) determined from IFT as a function of q (same color code used).

These results clearly support previous DLS and cryo-TEM observations. The amphiphiles self-assemble into a spherical micellar shape. SAXS data were also fitted using a spherical core-shell model for $(PMan)_8$-*b*-OI, $(PMan)_8$-*b*-Ric and $(PMan)_3$-*b*-Ric amphiphiles while applying a cylindrical core-shell model for $(PMan)_3$-*b*-OI, **Figure 4** (solid line). A compact hydrophilic mannose shell is surrounding a hydrophobic core, where the amphiphilic tail is placed (all the values obtained after the fitting are summarized in **Table S1**). In line with previous interfacial and bulk results, $(PMan)_8$-*b*-Ric and $(PMan)_8$-*b*-OI amphiphiles, with the same sugar $\overline{DP}$, self-assemble into spherical micelles with similar R_{shell} values of 27.3 and 27.7 Å, respectively. The ricinoleic tail, with a possibly favorable bent organization, leads to a smaller core characterized by a R_{core} of 15.0 Å,

while the oleic tail gives a R_{core} of 17.4 Å, explaining the smaller size of the (PMan)$_8$-*b*-Ric micelles. (PMan)$_3$-*b*-Ric, while showing a thinner sugar shell with a R_{shell} value of 20.8 Å, has a larger micellar size compared to (PMan)$_8$-*b*-Ric. Due to a more vertical orientation of the hydrophobic moiety, described by a R_{core} of 21.7 Å, (PMan)$_3$-*b*-Ric self-assembles into larger spherical micelles, in agreement with DLS results. (PMan)$_3$-*b*-OI cylindrical micelles were characterized by having a similar sugar R_{shell} than (PMan)$_3$-*b*-Ric, of 19.9 Å, while possessing a shorter R_{core} of 17.0 Å, in range of (PMan)$_8$-*b*-OI one. These tail results are in line with MM and MD simulations, as in **Figure S15**, where the ideal distances for every conformation are shown as a reference.

By using an inversion approach, the pair distance distribution functions (PDDFs) were also calculated, **Figure 4** (inner plot). A two-step function characteristic of a core-shell model is observed for all the surfactants. Such a two-step model gives an average idea of the size of the head groups at the outer shell, as well as information about the length of the chains at the inner shell[49]. Moreover, the intersection with the x-axis of the PDDF can give information about the size of the spherical micelles, which is two times the radius. Spherical micelles showed an increased average size, going from (PMan)$_8$-*b*-Ric to (PMan)$_8$-*b*-OI and (PMan)$_3$-*b*-Ric. All radii were in agreement with previous DLS results and confirmed the size values obtained after the core-shell fitting. As previously observed, (PMan)$_8$-*b*-OI is described by a thicker core region and a final micellar size compared to its (PMan)$_8$-*b*-Ric counterpart (**Figure 4a**). In contrast, while still a core-shell system, (PMan)$_3$-*b*-OI PDDF denoted a clear cylindrical conformation against (PMan)$_3$-*b*-Ric, which was spherical (**Figure 4b**). A pronounced peak in the low-r regime and an extended tail in the high-r side exhibits the typical feature of cylindrical nanoparticles[50]. Also, the flexible behavior of the cylindrical micelles can be elucidated, characterized by a non-linear decay of the PDDF to high-r values, which also denotes the average length of the micelles[49].

To attain a depth insight in the formation of the (PMan)$_3$-*b*-OI self-assembled cylindrical micelles, coarse-grained (CG) molecular dynamic (MD) simulations were performed. All the modelling

parameters and conditions used are summarized in **Figure S17-S18**. Note that the model is based on monodispersed ideal samples, but allows us to observe the average conformation of the amphiphile at this $\overline{DP}$. **Figure 5** snapshots depict the self-assembly process of the amphiphiles in time. Water beads were eliminated for a clear vision of the structures. The relationship between the molecular structure and its self-assembly have been accurately reported before by CG MDs[51]. From a randomly organized state, which represents the addition of the amphiphiles to an aqueous media at 0 ns, surfactants quickly started to reorganize in the form of small clusters, where the hydrophobic moieties avoid their contact with water (**Figure 5a**). The recombination of these aggregates led to the formation of the first stable assembly, spherical micelles, and the sugars formed a shell surrounding the hydrophobic tail (**Figure 5b**). In time, these spherical micelles came closer, merged, and lengthened into rod-like micelles (**Figure 5c**). Finally, the rod-like structure continued to interact with the rest of the spherical micelles, forming a final cylindrical micellar structure (**Figure 5d**). Note that the periodicity of the box denotes the connection of both sides of the cylindrical structure. A more quantitative analysis of the self-assembly process and the evolution of the average chain numbers of the aggregates is collected in **Figure S19**. In line with experimental DLS as well as SAXS results, $(PMan)_3$-*b*-OI amphiphiles self-assemble into more thermodynamically stable cylindrical micelles after the intermediate states of spherical and worm-like micelles.

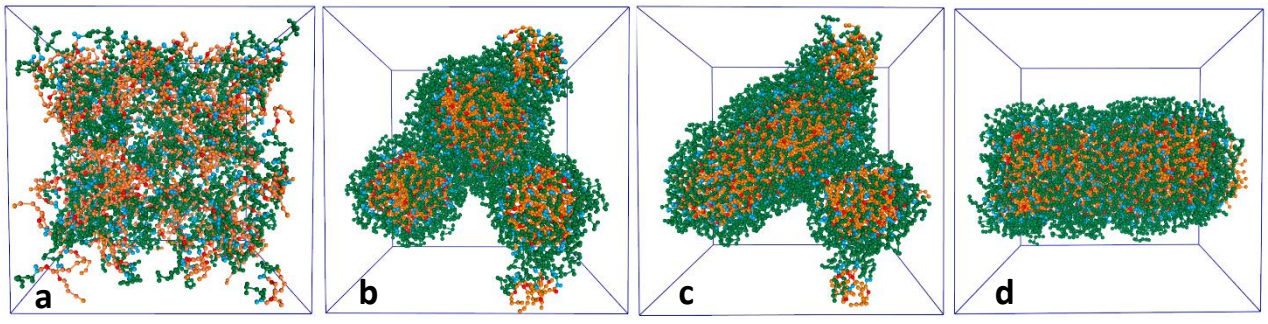

Figure 5. Representative snapshots of the cylindrical micelle formation processes at different time stages of $(PMan)_3$-*b*-OI at **(a)** 0 ns **(b)** 85 ns **(c)** 120 ns **(d)** 500 ns. For clarity, water beads are not shown.

The CG MD simulations also allowed the observation of the rod-like micelle formation. The detailed pathway is shown in **Figure 6**. Two micelles came closer to each other by their Brownian motion at the aqueous media (**Figure 6a**). As in the formation of a micelle, the amphiphiles interacted and the spherical shape of the micelle started to get deformed (**Figure 6b**). In time, the hydrophobic regions of the micelles met gradually (**Figure 6c**), and a final rod-like micelle structure was formed (**Figure 6d**). From these results, it can be inferred how, at early stages, $(PMan)_3$-*b*-OI self-assemble into initial spherical micelles that evolve into final more thermodynamically stable cylindrical ones.

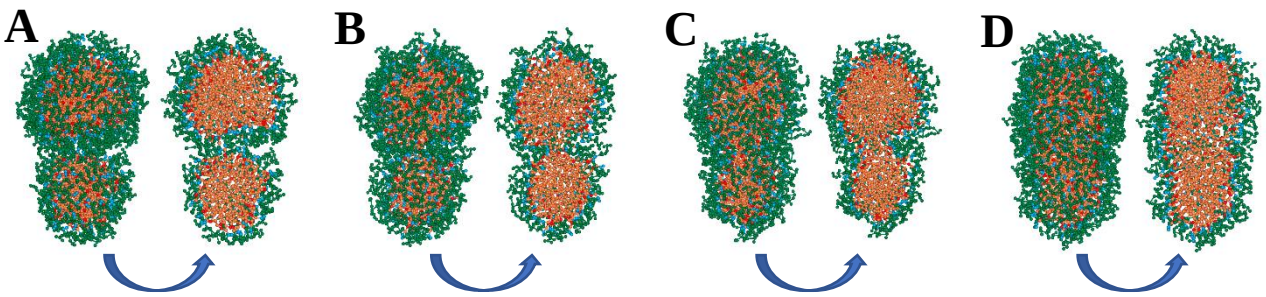

Figure 6. (a-d) Representative snapshots of the fusion process of two $(PMan)_3$-*b*-OI spherical micelles into one rod-like micelle.

4. Conclusions

Changes in the hydrophobic and hydrophilic moieties of the designed mannose-based amphiphiles are directly related to their final self-assembled structure at the 2D and 3D systems. Tiny tuning-up changes in the structure of the biobased amphiphiles can lead to the desired different self-assembly processes and resulting nanostructures. While an increase in the polysaccharide chain, from $(PMan)_3$ to $(PMan)_8$, does not affect the CMC, $(PMan)_8$ mannose derivatives at the air/water interface denoted higher γCMC values than $(PMan)_3$ ones, possibly due to larger polar head volumes and a less alkyl chain coverture at the surface[36]. Also, the presence of a hydroxyl group in the ricinoleic acid derivatives is suggested to act as a second hydrophilic moiety, promoting a reorganization of the hydrophobic region. The bending of the tail could be related to the decrease of the CMC and

γCMC values of the system[41]. Changes in the 3D self-assembly of the amphiphiles can also be observed in line with the interfacial studies. $(PMan)_8$-*b*-OI and $(PMan)_8$-*b*-Ric high $\overline{DP_n}$ mannose derivatives tend to form self-assembled spherical micellar structures. No change in the final structure was induced by the presence of a hydroxyl group at the hydrophobic moiety but a slight decrease in the core radius. $(PMan)_3$-*b*-Ric, characterized by a thinner sugar shell than $(PMan)_8$-*b*-Ric, self-assembles into spherical micelles with a thicker core due to the possible vertical orientation of the tails. In contrast, $(PMan)_3$-*b*-OI does it into cylindrical micelles. In line with previous reports and supported by CG MD, when no second hydrophilic moiety is present at the molecular structure, a lower hydrophilic head/hydrophobic tail volume ratio in the molecular structure leads to cylindrical micelles. Systems with a higher ratio, as $(PMan)_8$-*b*-OI, lead to spherical ones[43]. These conclusions offer interesting guidelines for the design of specific sugar-based self-assembled amphiphiles in a wide range of fields, broadening their supramolecular design and, more specifically, mannose-based ones. This edition process could be applied in biomedicine, to design nanocarriers, where spherical micelles are required due to lower circulation time in the human body[52] while cylindrical micelles are on demand due to their high aspect ratio and enhanced properties[12].

Associated Content

Supporting Information: synthesis procedure, pendant drop, dynamic light scattering measurements, cryo-TEM pictures, all-atom and coarse-grained modelling parameters and results. The following files are available free of charge: Supporting_Information (PDF)

Author Information

Corresponding Authors

* pgomezargud@enscbp.fr (P. A.)

* Sebastien.Lecommandoux@enscbp.fr (S. L.)

Author Contributions

The manuscript was written through contributions of all authors. All authors have given approval to the final version of the manuscript. ‡These authors contributed equally.

ORCID

Pablo G. Argudo - 0000-0001-5964-727X

Léa Spitzer - 0000-0002-0530-1262

François Jerome - 0000-0002-8324-0119

Henri Cramail - 0000-0001-9798-6352

Luis Camacho - 0000-0002-2141-1437

Sébastien Lecommandoux - 0000-0003-0465-8603

Acknowledgments

P.G.A., L.S., H.C., S.L. acknowledge the Centre National de la Recherche Scientifique, the Région Nouvelle Aquitaine, and Université de Bordeaux. F.G. is thankful to the Université de Poitiers. L.C. is grateful for financial support from the Andalusian Government (Consejería de Economía, Conocimiento, Empresas y Universidades, Junta de Andalucía) of Spain UCO-1263193 Project. Ahmed Bentaleb and François Dole (Centre de Recherche Paul Pascal, CRPP) are gratefully acknowledged for their support respectively for SAXS and ITC experiments. Jean-Michel Guigner (Sorbonne Université) and Amelie Vax-Webber (LCPO) are gratefully acknowledged for their support, respectively for cryo-TEM and SEC experiments.

References

(1) Grimaldi, N.; Andrade, F.; Segovia, N.; Ferrer-Tasies, L.; Sala, S.; Veciana, J.; Ventosa, N. Lipid-Based Nanovesicles for Nanomedicine. *Chem. Soc. Rev.* **2016**, *45* (23), 6520–6545. https://doi.org/10.1039/c6cs00409a.

(2) Sachse, A.; García-Martínez, J. Surfactant-Templating of Zeolites: From Design to Application. *Chem. Mater.* **2017**, *29* (9), 3827–3853. https://doi.org/10.1021/acs.chemmater.7b00599.

(3) Hardy, D.; Bill, R. M.; Jawhari, A.; Rothnie, A. J. Overcoming Bottlenecks in the Membrane Protein Structural Biology Pipeline. *Biochem. Soc. Trans.* **2016**, *44* (3), 838–844. https://doi.org/10.1042/BST20160049.

(4) Yang, J. Viscoelastic Wormlike Micelles and Their Applications. *Curr. Opin. Colloid Interface Sci.* **2002**, *7* (5–6), 276–281. https://doi.org/10.1016/S1359-0294(02)00071-7.

(5) Rehage, H.; Hoffmann, H. Rheological Properties of Viscoelastic Surfactant Systems. *J. Phys. Chem.* **1988**, *92* (16), 4712–4719. https://doi.org/10.1021/j100327a031.

(6) Raffa, P.; Wever, D. A. Z.; Picchioni, F.; Broekhuis, A. A. Polymeric Surfactants: Synthesis, Properties, and Links to Applications. *Chem. Rev.* **2015**, *115* (16), 8504–8563. https://doi.org/10.1021/cr500129h.

(7) Hayes, D.; Solaiman, D.; Ashby, R. *Biobased Surfactants*, 2nd Editio.; Academic Press and AOCS Press, 2019.

(8) Fernández-Peña, L.; Guzmán, E.; Leonforte, F.; Serrano-Pueyo, A.; Regulski, K.; Tournier-Couturier, L.; Ortega, F.; Rubio, R. G.; Luengo, G. S. Effect of Molecular Structure of Eco-Friendly Glycolipid Biosurfactants on the Adsorption of Hair-Care Conditioning Polymers. *Colloids Surfaces B Biointerfaces* **2020**, *185* (June 2019), 110578. https://doi.org/10.1016/j.colsurfb.2019.110578.

(9) Celligoi, M. A. P. C.; Silveira, V. A. I.; Hipólito, A.; Caretta, T. O.; Baldo, C. Sophorolipids: A Review on Production and Perspectives of Application in Agriculture. *Spanish J. Agric. Res.* **2020**, *18* (3), 1–10. https://doi.org/10.5424/sjar/2020183-15225.

(10) Esumi, K.; Ueno, M. *Structure-Performance Relationships in Surfactants*; 2003.

(11) Vonnemann, J.; Sieben, C.; Wolff, C.; Ludwig, K.; Böttcher, C.; Herrmann, A.; Haag, R.

Virus Inhibition Induced by Polyvalent Nanoparticles of Different Sizes. *Nanoscale* **2014**, *6* (4), 2353. https://doi.org/10.1039/c3nr04449a.

(12) Ridolfo, R.; Tavakoli, S.; Junnuthula, V.; Williams, D. S.; Urtti, A.; Van Hest, J. C. M. Exploring the Impact of Morphology on the Properties of Biodegradable Nanoparticles and Their Diffusion in Complex Biological Medium. *Biomacromolecules* **2021**, *22* (1), 126–133. https://doi.org/10.1021/acs.biomac.0c00726.

(13) Voggel, M.; Meinusch, R. M.; Siewert, V.; Kunkel, M.; Wittmann, V.; Polarz, S. Sweet Surfactants: Packing Parameter-Invariant Amphiphiles as Emulsifiers and Capping Agents for Morphology Control of Inorganic Particles. *Soft Matter* **2018**, *14* (35), 7214–7227. https://doi.org/10.1039/c8sm01091a.

(14) Lu, H.; Pezron, I.; Gaudin, T.; Drelich, A. Non-Equilibrium Micelles Formed by Sugar-Based Surfactants under Their Krafft Temperature. *Colloids Surfaces A Physicochem. Eng. Asp.* **2018**, *540*, 167–176. https://doi.org/10.1016/j.colsurfa.2017.12.053.

(15) Larsson, J.; Williams, A. P.; Wahlgren, M.; Porcar, L.; Ulvenlund, S.; Nylander, T.; Tabor, R. F.; Sanchez-Fernandez, A. Shear-Induced Nanostructural Changes in Micelles Formed by Sugar-Based Surfactants with Varied Anomeric Configuration. *J. Colloid Interface Sci.* **2022**, *606*, 328–336. https://doi.org/10.1016/j.jcis.2021.08.007.

(16) Rosselgong, J.; Chemin, M.; Almada, C. C.; Hemery, G.; Guigner, J. M.; Chollet, G.; Labat, G.; Da Silva Perez, D.; Ham-Pichavant, F.; Grau, E.; Grelier, S.; Lecommandoux, S.; Cramail, H. Synthesis and Self-Assembly of Xylan-Based Amphiphiles: From Bio-Based Vesicles to Antifungal Properties. *Biomacromolecules* **2019**, *20* (1), 118–129. https://doi.org/10.1021/acs.biomac.8b01210.

(17) Zago, E.; Joly, N.; Chaveriat, L.; Lequart, V.; Martin, P. Enzymatic Synthesis of Amphiphilic Carbohydrate Esters: Influence of Physicochemical and Biochemical Parameters. *Biotechnol. Reports* **2021**, *30*, e00631. https://doi.org/10.1016/j.btre.2021.e00631.

(18) Gaudin, T.; Rotureau, P.; Pezron, I.; Fayet, G. Investigating the Impact of Sugar-Based Surfactants Structure on Surface Tension at Critical Micelle Concentration with Structure-Property Relationships. *J. Colloid Interface Sci.* **2018**, *516*, 162–171. https://doi.org/10.1016/j.jcis.2018.01.051.

(19) Mittal, A.; Krishna; Aarti; Prasad, S.; Mishra, P. K.; Sharma, S. K.; Parshad, B. Self-Assembly of Carbohydrate-Based Small Amphiphiles and Their Applications in Pathogen

Inhibition and Drug Delivery: A Review. *Mater. Adv.* **2021**, *2* (11), 3459–3473. https://doi.org/10.1039/D0MA00916D.

(20) Gaudin, T.; Rotureau, P.; Pezron, I.; Fayet, G. New QSPR Models to Predict the Critical Micelle Concentration of Sugar-Based Surfactants. *Ind. Eng. Chem. Res.* **2016**, *55* (45), 11716–11726. https://doi.org/10.1021/acs.iecr.6b02890.

(21) Lea Spitzer; Lecommandoux, S.; Cramail, H.; Jérôme, F. Sequential Acid-Catalyzed Alkyl Glycosylation and Oligomerization of Unprotected Carbohydrates. *Green Chem.* **2021**. https://doi.org/10.1039/D0GC04198J.

(22) Dalle Vedove, E.; Costabile, G.; Merkel, O. M. Mannose and Mannose-6-Phosphate Receptor–Targeted Drug Delivery Systems and Their Application in Cancer Therapy. *Adv. Healthc. Mater.* **2018**, *7* (14), 1–19. https://doi.org/10.1002/adhm.201701398.

(23) Hu, X.; Shi, Y.; Zhang, P.; Miao, M.; Zhang, T.; Jiang, B. D-Mannose: Properties, Production, and Applications: An Overview. *Compr. Rev. Food Sci. Food Saf.* **2016**, *15* (4), 773–785. https://doi.org/10.1111/1541-4337.12211.

(24) Martinez-Pomares, L. The Mannose Receptor. *J. Leukoc. Biol.* **2012**, *92* (6), 1177–1186. https://doi.org/10.1189/jlb.0512231.

(25) Argudo, P. G.; Contreras-Montoya, R.; Álvarez de Cienfuegos, L.; Cuerva, J. M.; Cano, M.; Alba-Molina, D.; Martín-Romero, M. T.; Camacho, L.; Giner-Casares, J. J. Unravelling the 2D Self-Assembly of Fmoc-Dipeptides at Fluid Interfaces. *Soft Matter* **2018**, *14* (46), 9343–9350. https://doi.org/10.1039/c8sm01508b.

(26) Li, L.; Sun, R.; Zheng, R. Tunable Morphology and Functionality of Multicomponent Self-Assembly: A Review. *Mater. Des.* **2021**, *197*, 109209. https://doi.org/10.1016/j.matdes.2020.109209.

(27) Berry, J. D.; Neeson, M. J.; Dagastine, R. R.; Chan, D. Y. C.; Tabor, R. F. Measurement of Surface and Interfacial Tension Using Pendant Drop Tensiometry. *J. Colloid Interface Sci.* **2015**, *454*, 226–237. https://doi.org/10.1016/j.jcis.2015.05.012.

(28) Hishida, M.; Kaneko, Y.; Okuno, M.; Yamamura, Y.; Ishibashi, T. A.; Saito, K. Communication: Salt-Induced Water Orientation at a Surface of Non-Ionic Surfactant in Relation to a Mechanism of Hofmeister Effect. *J. Chem. Phys.* **2015**, *142* (17). https://doi.org/10.1063/1.4919664.

(29) Penfold, J.; Thomas, R. K.; Dong, C. C.; Tucker, I.; Metcalfe, K.; Golding, S.; Grillo, I. Equilibrium Surface Adsorption Behavior in Complex Anionic/Nonionic Surfactant Mixtures. *Langmuir* **2007**, *23* (20), 10140–10149. https://doi.org/10.1021/la701151m.

(30) Neimert-Andersson, K.; Sauer, S.; Panknin, O.; Borg, T.; Söderlind, E.; Somfai, P. Synthesis of New Sugar-Based Surfactants and Evaluation of Their Hemolytic Activities. *J. Org. Chem.* **2006**, *71* (9), 3623–3626. https://doi.org/10.1021/jo051904b.

(31) Milkereit, G.; Garamus, V. M.; Veermans, K.; Willumeit, R. Structures of Micelles Formed by Synthetic Alkyl Glycosides with Unsaturated Alkyl Chains. *J. Colloid Interface Sci.* **2005**, *284*, 704–713. https://doi.org/10.1016/j.jcis.2004.10.039.

(32) Minamikawa, H.; Hato, M. Headgroup Effects on Phase Behavior and Interfacial Properties of β-3,7-Dimethyloctylglycoside/Water Systems. *Chem. Phys. Lipids* **2005**, *134* (2), 151–160. https://doi.org/10.1016/j.chemphyslip.2005.01.001.

(33) Lu, B.; Vayssade, M.; Miao, Y.; Chagnault, V.; Grand, E.; Wadouachi, A.; Postel, D.; Drelich, A.; Egles, C.; Pezron, I. Physico-Chemical Properties and Cytotoxic Effects of Sugar-Based Surfactants: Impact of Structural Variations. *Colloids Surfaces B Biointerfaces* **2016**, *145*, 79–86. https://doi.org/10.1016/j.colsurfb.2016.04.044.

(34) Garofalakis, G.; Murray, B. S.; Sarney, D. B. Surface Activity and Critical Aggregation Concentration of Pure Sugar Esters with Different Sugar Headgroups. *J. Colloid Interface Sci.* **2000**, *229* (2), 391–398. https://doi.org/10.1006/jcis.2000.7035.

(35) Vanaken, T.; Foxall-Vanaken, S.; Castleman, S.; Ferguson-Miller, S. [3] Alkyl Glycoside Detergents: Synthesis and Applications to the Study of Membrane Proteins. In *Methods in Enzymology*; 1986; Vol. 125, pp 27–35. https://doi.org/10.1016/S0076-6879(86)25005-3.

(36) Gaudin, T.; Lu, H.; Fayet, G.; Berthauld-Drelich, A.; Rotureau, P.; Pourceau, G.; Wadouachi, A.; Van Hecke, E.; Nesterenko, A.; Pezron, I. Impact of the Chemical Structure on Amphiphilic Properties of Sugar-Based Surfactants: A Literature Overview. *Adv. Colloid Interface Sci.* **2019**, *270*, 87–100. https://doi.org/10.1016/j.cis.2019.06.003.

(37) Garofalakis, G.; Murray, B. S.; Sarney, D. B. Surface Activity and Critical Aggregation Concentration of Pure Sugar Esters with Different Sugar Headgroups. *J. Colloid Interface Sci.* **2000**, *229* (2), 391–398. https://doi.org/10.1006/jcis.2000.7035.

(38) Seelig, A.; Seelig, J. Effect of a Single Cis Double Bond on the Structure of a Phospholipid

Bilayer. *Biochemistry* **1977**, *16* (1), 45–50. https://doi.org/10.1021/bi00620a008.

(39) Siegel, S.; Vollhardt, D.; Cadenhead, D. A. Effect of the Hydroxy Group Position on the Monolayer Characteristics of Hydroxypalmitic Acids. *Colloids Surfaces A Physicochem. Eng. Asp.* **2005**, *256* (1 SPEC. ISS.), 9–15. https://doi.org/10.1016/j.colsurfa.2004.09.040.

(40) Bhadani, A.; Iwabata, K.; Sakai, K.; Koura, S.; Sakai, H.; Abe, M. Sustainable Oleic and Stearic Acid Based Biodegradable Surfactants. *RSC Adv.* **2017**, *7* (17), 10433–10442. https://doi.org/10.1039/C6RA27036K.

(41) Nagarajan, M. K.; Shah, J. P. Conformation and Phase Transitions in Monolayers of Some C18 Fatty Acids Containing a Hydratable Functional Group in Their Alkyl Chains. *J. Colloid Interface Sci.* **1981**, *80* (1), 7–19. https://doi.org/10.1016/0021-9797(81)90154-5.

(42) Shinde, N.; Narayan, K. S. Studies on Sodium Ricinoleate. 1. Adsorption and Aggregation Behavior. *J. Phys. Chem.* **1992**, *96* (12), 5160–5165. https://doi.org/10.1021/j100191a075.

(43) Israelachvili, J. N.; Mitchell, D. J.; Ninham, B. W. Theory of Self-Assembly of Hydrocarbon Amphiphiles into Micelles and Bilayers. *J. Chem. Soc. Faraday Trans. 2 Mol. Chem. Phys.* **1976**, *72*, 1525–1568. https://doi.org/10.1039/F29767201525.

(44) Tian, Q.; Zhang, D.; Li, N.; Henderson, M. J.; Li, Q.; Royal, G.; Courtois, J.; Yan, M.; Zhu, Z.; Almásy, L. Structural Study of Polystyrene- b-Poly(Acrylic Acid) Micelles Complexed with Uranyl: A SAXS Core-Shell Model Analysis. *Langmuir* **2020**, *36* (17), 4820–4826. https://doi.org/10.1021/acs.langmuir.9b03934.

(45) Bauer, C.; Bauduin, P.; Girard, L.; Diat, O.; Zemb, T. Hydration of Sugar Based Surfactants under Osmotic Stress: A SAXS Study. *Colloids Surfaces A Physicochem. Eng. Asp.* **2012**, *413*, 92–100. https://doi.org/10.1016/j.colsurfa.2012.03.006.

(46) Burchard, W. Static and Dynamic Light Scattering from Branched Polymers and Biopolymers. *Light Scatt. from Polym.* **2007**, 1–124. https://doi.org/10.1007/3-540-12030-0_1.

(47) Chécot, F.; Brûlet, A.; Oberdisse, J.; Gnanou, Y.; Mondain-Monval, O.; Lecommandoux, S. Structure of Polypeptide-Based Diblock Copolymers in Solution: Stimuli-Responsive Vesicles and Micelles. *Langmuir* **2005**, *21* (10), 4308–4315. https://doi.org/10.1021/la0468500.

(48) Le Hellaye, M.; Fortin, N.; Guilloteau, J.; Soum, A.; Lecommandoux, S.; Guillaume, S. M.

Biodegradable Polycarbonate-b-Polypeptide and Polyester-b-Polypeptide Block Copolymers: Synthesis and Nanoparticle Formation towards Biomaterials. *Biomacromolecules* **2008**, *9* (7), 1924–1933. https://doi.org/10.1021/bm8001792.

(49) Pérez, B.; Coletta, A.; Pedersen, J. N.; Petersen, S. V.; Periole, X.; Pedersen, J. S.; Sessions, R. B.; Guo, Z.; Perriman, A.; Schiøtt, B. Insight into the Molecular Mechanism behind PEG-Mediated Stabilization of Biofluid Lipases. *Sci. Rep.* **2018**, *8* (1), 1–13. https://doi.org/10.1038/s41598-018-29871-z.

(50) Shrestha, L. K.; Sharma, S. C.; Sato, T.; Glatter, O.; Aramaki, K. Small-Angle X-Ray Scattering (SAXS) Study on Nonionic Fluorinated Micelles in Aqueous System. *J. Colloid Interface Sci.* **2007**, *316* (2), 815–824. https://doi.org/10.1016/j.jcis.2007.08.005.

(51) Wang, P.; Pei, S.; Wang, M.; Yan, Y.; Sun, X.; Zhang, J. Coarse-Grained Molecular Dynamics Study on the Self-Assembly of Gemini Surfactants: The Effect of Spacer Length. *Phys. Chem. Chem. Phys.* **2017**, *19* (6), 4462–4468. https://doi.org/10.1039/c6cp07690d.

(52) Cao, C.; Zhang, L.; Kent, B.; Wong, S.; Garvey, C. J.; Stenzel, M. H. The Protein Corona Leads to Deformation of Spherical Micelles. *Angew. Chemie - Int. Ed.* **2021**, *60* (18), 10342–10349. https://doi.org/10.1002/anie.202101129.

Graphic for Table of Content (8.5 cm x 4.75 cm)